



Physical properties of multifunctional TM-doped ZnO nanorods and their photocatalytic and anti-bacterial activities

Yasir Zaman¹ · Muhammad Zahid Ishaque¹ · Yasir Yousaf¹ · Muhammad Shahzad¹ · Abu Bakar Siddique² · Muhammad Imran Arshad³ · Muhammad Sajid⁴ · Nisar Ali⁵ · Ghulam Nabi⁶

Received: 22 November 2022 / Accepted: 31 July 2023 / Published online: 10 August 2023
© The Author(s), under exclusive licence to Springer-Verlag GmbH Germany, part of Springer Nature 2023

Abstract

Dilute magnetic semiconductor $Zn_{1-x}Cu_xO$ ($x=0, 1.5, 3.0,$ and 4.5%) nanorods were prepared by hydrothermal method. The impact of dopant concentration on the physical properties was investigated along with the anti-bacterial and photocatalytic activities. Synthesis of ZnO nanorods was confirmed by the characteristic band at 380 nm in UV–Visible spectra of the synthesized samples. A red shift in absorbance spectra was observed from 380 to 465 nm with an increase in dopant concentration. The hexagonal wurtzite geometry and rod-like morphology of Cu-doped ZnO nanorods having an average size of 29 nm were confirmed by X-ray diffraction analysis (XRD) and scanning electron microscopy (SEM), respectively. An increase in the crystallinity of the material was observed with an increase in the dopant (Cu) ratio without any alteration in geometry. EDX analysis was used to confirm the purity of samples. FTIR spectra were recorded to explore the functional group present in samples. The hysteresis loop drawn by a vibrating-sample magnetometer (VSM) was utilized to analyze the ferromagnetic behavior. As-synthesized pure and Cu–ZnO nanorods were evaluated for their photocatalytic behavior for the photodegradation of methyl orange (MO) dye. $Zn_{1-x}Cu_xO$ with $x=4.5\%$, pH 3, and catalyst dosage of 0.5 g has shown the maximum efficiency. Results elucidated $>81\%$ degradation of MO dye with a rate constant (k) value of $-1.930 \times 10^{-2} \text{ min}^{-1}$ in just 90 min of exposure to a visible light source. ZnO nanorods have also exhibited anti-bacterial potential against gram-positive and gram-negative strains of bacteria. However, smaller size nanorods were found more effective to suppress the growth of gram-negative bacteria. A slight decrease (11%) in catalytic potential was observed in the 5th cycle during recycling and reuse experiments.

Keywords Cu-doped ZnO nanorods · Doping · Nanorods · Photocatalysis · Anti-bacterial activity · Regeneration studies · The effect of pH and catalyst dosage

Introduction

During the last two decades, in nanomaterial science, noble metals, ferrites, and metal oxides have gained considerable attention from researchers due to their outstanding electrical and magnetic properties (Zaman et al. 2022; Ali et al.

2015). ZnO is a unique metal oxide material possessing novel characteristics, such as an n-type semiconductor, low energy band gap (3.37 eV), and larger excitation binding energy (60 meV) (Kumbhakar et al. 2021). In microelectronic appliances that are in recent demand of time, it is vital to incorporate the spin and charge of an electron as an additional degree of freedom in electronic/spintronic gadgets. The desired property can be designed by synthesizing dilute magnetic semiconductor (DMS) NPs having room temperature ferromagnetism (RTF). These DMS-NPs have excellent dielectric and electrical abilities with varying frequencies of applied electric field and temperature (Ramírez et al. 2021). Mostly, transition metals were used for the doping of ZnO in order to improve the effectiveness of ZnO NPs (Shkir et al. 2022). For the synthesis of these NPs, a variety of methods can be adopted, such as hydrothermal (Wu et al.

Responsible Editor: Sami Rtimi

Highlights

- Construction of pure and copper-doped zinc oxide semiconductor nanorods.
- Hydrothermal process followed by solution mixing.
- Copper-doped zinc oxide for photocatalytic applications.
- Nanorods were more active toward gram-negative strains of bacteria.

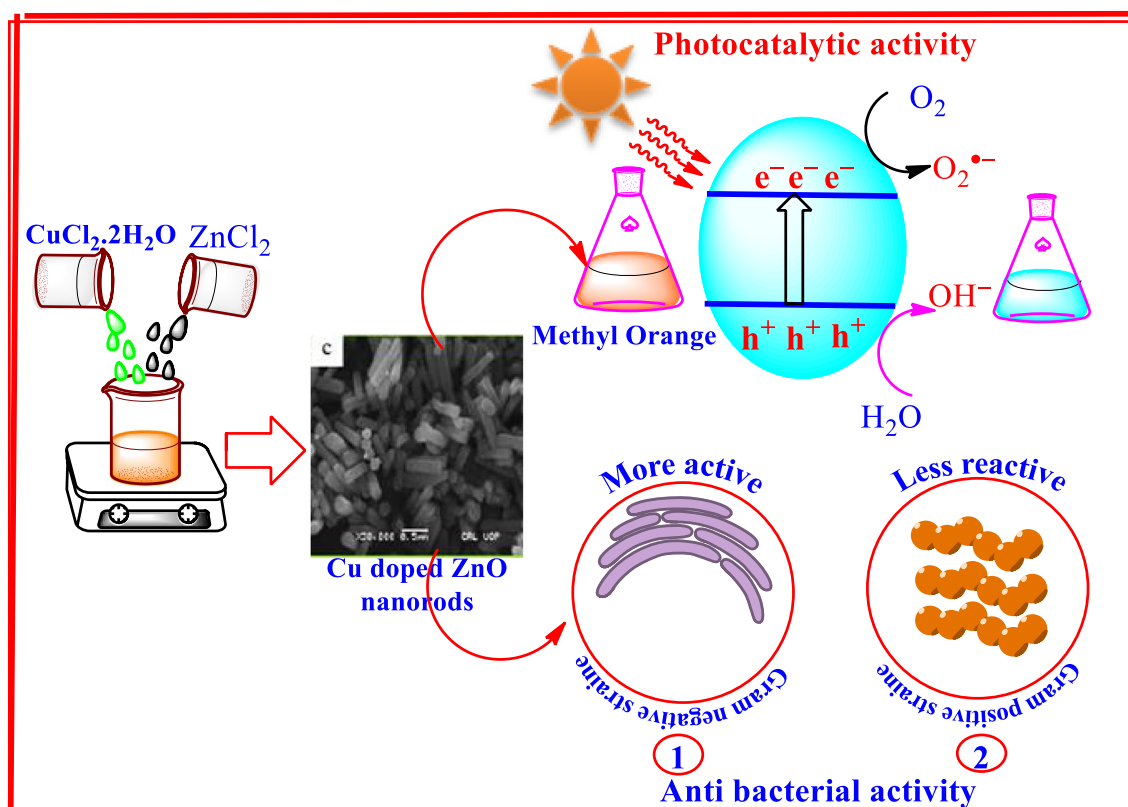
Extended author information available on the last page of the article

2021), sol–gel (Naik et al. 2020), co-precipitation (Kant et al. 2021), and auto-combustion method (Kotresh et al. 2021). However, the hydrothermal method is preferred to obtain uniform morphology and size-controlled crystalline nanoparticles. Additionally, this technique is robust, cheap, and uses water as a solvent (Tariq et al. 2023; Gan et al. 2020).

Owing to the exclusive properties, ZnO and doped oxides have been explored extensively in many fields such as photocatalysis (Jabbar et al. 2022; Muktaridha et al. 2021; Ali et al. 2021a, b; Ali et al. 2020), anti-bacterial agents (Ali et al. 2021a, b; Salam et al. 2021), gas sensors (Mortezagholi et al. 2022), solar cells (Çolak and Karaköse 2022), varistor (Ge et al. 2021), and cancer treatment (Shi et al. 2021). These days, with a growing number of industries, industrial waste became a challenging and critical issue for the survival of the ecosystem. Plastic, paper, food, textile, and other industries use hazardous dyes, such as Congo red, methyl orange, and direct black organic dye for the preparation of their products (Ahmed et al. 2021). The liquid waste of these industries is discharged into rivers, lakes, seas, and groundwater without any purification. This contaminated liquid pollutes the storage of water and affects the life of amphibians (Sajid et al. 2022; Guoliang et al. 2022). The researcher tried many chemical and physical methods for

the purification of contaminated water, but these were not feasible, either in terms of cost or effectiveness. Metal oxide NPs played an important role in dye degradation because of their large surface defects (Anjum et al. 2021). It is a very effective technique because it has an appropriate band gap and absorbs UV or visible light and generates many electron–hole pairs for photocatalysis. ZnO NPs were proven as a good photocatalyst and the photocatalyst activity of ZnO NPs increased as they doped with transition metals, because the dopant increases the surface defect and decreases the band gap of NPs (Usman et al. 2022; Maqbool et al. 2023; Sattara et al. 2023).

ZnO NPs can be used as an anti-bacterial agent because they can suppress the growth of bacterial strains effectively. Bacterial infection is very dangerous to health; sometimes it is too fatal and becomes a cause of death. Bacteria are in the micrometer range and their cell wall is porous, through which nanoparticles can easily pass and penetrate the cell of bacteria (Zaman et al. 2022). Generation of reactive oxygen species (ROS), releasing of ions of NPs, and accumulation of NPs are three mechanisms through which ZnO NPs affect the normal functioning of the cell of bacteria. In all these mechanisms, protein and DNA are destroyed by NPs which cause the growth inhibition or death of bacteria (Jabbar et al. 2022).



Scheme 1 Photocatalytic and anti-bacterial activity of Cu-doped ZnO nanorods

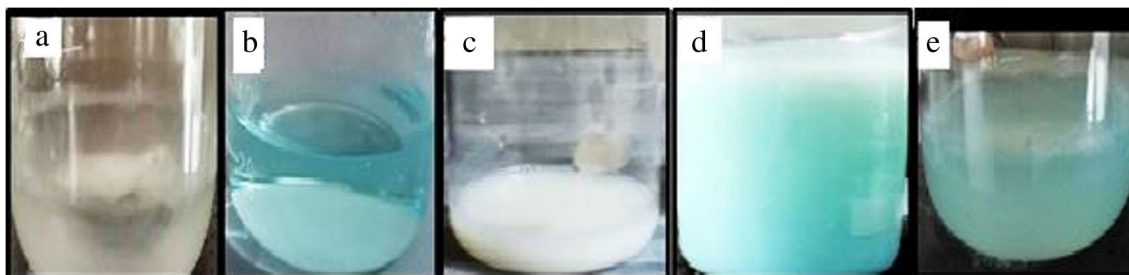


Fig. 1 Solution color of **a** Zn precursor, **b** Cu precursor, **c** pure ZnO, **d** Cu-doped ZnO on achieving desired pH, and **e** finally prepared Cu-doped ZnO

In the present research work, we have reported the synthesis of Cu-doped ZnO nanorods by hydrothermal method with variable dopant concentrations. Subsequent to the characterization of NPs, these have been subjected to estimation of their electrical and magnetic properties. Ultimately, pure and doped ZnO NPs have been evaluated for their photocatalytic potential to degrade MO dye and suppress the growth of various bacterial strains as shown in Scheme 1. The effect of pH, light intensity, and catalyst dosage on the photodegradation of MO dye has been studied to optimize the reaction conditions. Furthermore, the reusability of the developed catalyst was evaluated in repeated cycles by measuring the % degradation of dye in each cycle successively. To the best of our knowledge, this composition of nanostructures has not been studied so far for these applications.

Experimental

Materials and methods

Analytical grade zinc chloride ($\text{ZnCl}_2 \cdot 2\text{H}_2\text{O}$), sodium hydroxide (NaOH), and copper (II) chloride dihydrate were purchased from Riedel–deHaen, Honeywell-Fluka®, and Sigma Aldrich, respectively. Powder XRD (PXRD) analysis was carried out by XRD (JDX-3532, JEOL, Japan) with Cu-K α lines (wavelength 1.5418 Å). SEM (JSM5910, JEOL, Japan) having maximum magnification and resolving power (300,000X and 2.3 nm) was used to capture the pictures of samples for morphological analysis of samples. The UV–Visible (Shimadzu Japan, Pharmaspec-1700) was used to record the absorbance spectra in the range of 200 to 800 nm. LCR meter, Keithley I–V measurement (model 2100) was used to measure the electrical properties of samples.

Synthesis of $\text{Zn}_{1-x}\text{Cu}_x\text{O}$ nanorods

Pure and copper-doped ZnO NPs were synthesized by hydrothermal method. For the preparation of pure ZnO nanorods, 2 M solutions of NaOH were added dropwise in 20 mL of

0.4 M solution of $\text{ZnCl}_2 \cdot 2\text{H}_2\text{O}$ until pH 9 was achieved with constant stirring. After 2 h, the colloidal system was centrifuged for 30 min at 1000 rpm. Subsequently, the mixture was filtered, and the solid was dried at 60 °C. The dried sample was stored in an airtight bottle for further analysis and application.

Cu-doped ZnO NPs ($\text{Zn}_{1-x}\text{Cu}_x\text{O}$ at $x = 1.5\%$, 3.0% , and 4.5%) were prepared by the same method by the addition of desired dopant solution of $\text{CuCl}_2 \cdot 2\text{H}_2\text{O}$. The prepared solution with different colors is shown in Fig. 1.

Photocatalytic activity

The photocatalytic potential of samples was evaluated for the decomposition of hazardous dye, i.e., MO, by exposure of samples under a visible light source (solar simulator, 300 W) following the previously reported method (Ishaque et al. 2023; Ali et al. 2023). Briefly, a 20 ppm solution of MO dye was prepared by dissolving 20 mg of dye in 1000 mL of distilled water. In 100 mL of dye solution, the desired amount of catalyst was added and the flask was kept in the dark for 20 min to develop adsorption–desorption equilibria. Subsequently, each sample was exposed to the visible light source, and absorbance spectra (at $\lambda_{\text{max}} = 468$ nm) were recorded after every 10 min by eluting out 3 mL of sample solution from the mixture. Dye decomposition (%) was measured using Eq. 1 by utilizing the decrease in absorbances of samples after regular intervals.

$$\% \text{ Dye degradation} = \frac{C_o - C_i}{C_o} \times 100 \quad (1)$$

where C_o is the initial concentration of MO dye and C_i is the concentration of dye after regular time intervals under exposure to light. A schematic decrease in absorbance with the passage of time is represented in Fig. 2.

The effect of pH, catalyst dosage, and intensity of light on the catalytic efficiency of the catalyst were determined by varying the pH in the range of 3 to 11, catalyst dosage from

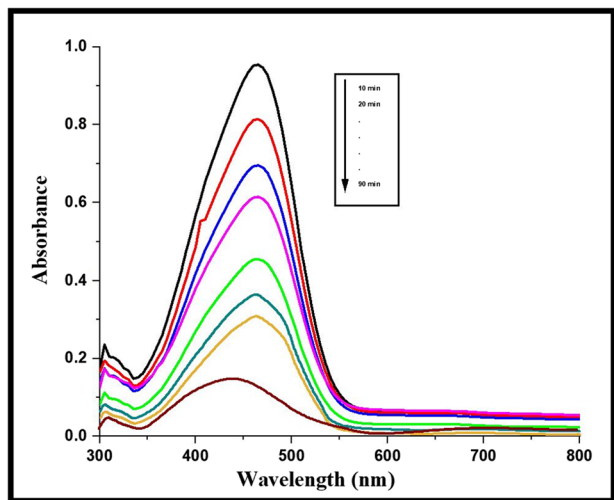


Fig. 2 Decrease in absorbance of light by nanorods with the passage of time

0.1 to 1 g, and light intensity by varying the distance from the lamp. For the determination of the effect of one parameter, other variables were kept constant at optimum values.

Disk diffusion assay

The disk diffusion method was used to evaluate the anti-bacterial potential of as-synthesized samples as reported in the literature (Zaman et al. 2023; Siddique et al 2022). Briefly, four bacterial strains, two gram-positive (*Staphylococcus aureus*, *Bacillus subtilis*) and two gram-negative (*Escherichia coli*, *Pasteurella multocida*), were grown in the nutrient agar solution (10 g/500 mL) for 24 h at 4 °C. Fresh agar nutrient broth solution (3 g/100 mL) was prepared by heating

on a water bath and poured in the sterilized Petri dishes on cooling. pH 7 of the medium was maintained throughout the process. Bacterial strains were added to Petri dishes as a source of seedlings. After the solidification of the agar, sterilized paper disks loaded with a solution of samples in DMSO (1 mg/mL) were placed on the agar surface. Rifampicin was used as a positive control. Petri dishes were placed in an incubator for 24 h at 37 °C. Subsequently, the zone of inhibition of each disk was measured in millimeters (mm).

Statistical analysis

Triplicate analysis was carried out for each photocatalytic and anti-bacterial test. The results were analyzed statistically by ANOVA. Statistical significance was accepted at a level of $p < 0.05$. All the results were reported as mean \pm SD.

Results and discussion

Optical properties

The absorbance spectra of pure ZnO and doped ZnO NPs recorded by a UV–Visible spectrophotometer revealed the synthesis of ZnO NPs by the appearance of a characteristic peak at 380 nm. A red shift in λ_{max} was observed from 380 to 465 nm with an increase of dopant concentration from 0.0 to 4.5% as shown in Fig. 3(a). This shift was attributed to the plasmonic effect of dopant noble metal atoms in nanorods. Copper atoms contain free electrons that are scattered on the surface of nanorods and can easily interact and absorb the interacting light radiations. Moreover, the broadening of the absorption band also occurs due to the surface plasmon resonance effect (Saber et al. 2020).

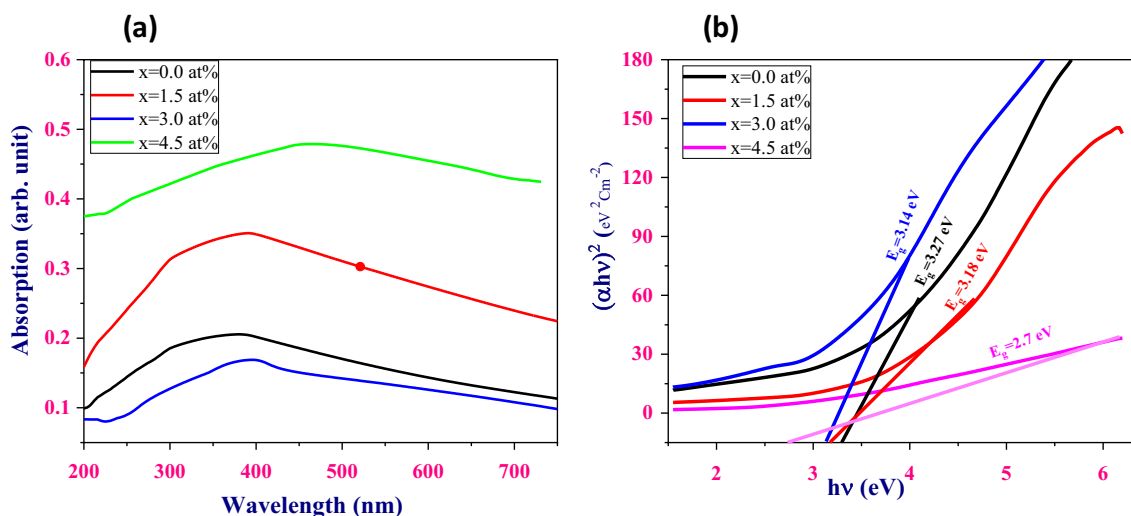


Fig. 3 a UV–Vis spectrum for Cu-doped ZnO nanorods. b Tauc’s plot for Cu-doped ZnO nanorods

Absorbance spectra have been utilized to calculate the energy band gap of nanorods using Tauc's relation as shown in Eq. 2 (Neamen 1992).

$$\alpha hv = A(hv - E_g)^2 \quad (2)$$

For bulk ZnO semiconductors, the optical band gap is 3.37 eV while it reduces to 3.27 eV in the case of ZnO nanorods due to a decrease in particle size. The optical band gap was decreased gradually with an increase of dopant concentration from 3.18 to 3.14 eV and then to 2.7 eV for $x = 1.5, 3.0,$ and 4.5% , respectively (Fig. 3(b)). This effect is because the free electrons of copper can easily absorb light and shift to the conduction band of ZnO in addition to the shifting of electrons from the valence band to the conduction band. High surface area and improved interaction of light are major reasons for the better catalytic and solar applications of nanomaterials.

FTIR spectra

FTIR spectrum was recorded to get information about the purity and functional groups present in the synthesized nanomaterial. Prominent peaks corresponding to the Zn–O bond were found in the region of $400\text{--}500\text{ cm}^{-1}$ consistent with the literature (Nagaraju et al. 2017). No additional peaks were found except the O–H broad peak in the region of $3200\text{--}3400\text{ cm}^{-1}$, which proved the purity of the samples. The comparative FTIR of the samples is shown in Fig. 4.

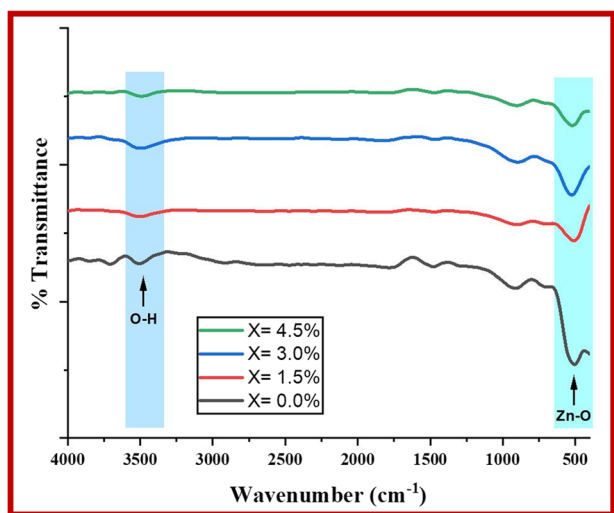


Fig. 4 FTIR spectra of $\text{Zn}_{1-x}\text{Cu}_x\text{O}$ with varying dopant concentration

Crystal structure and surface morphology

The crystal structure and phases of samples were determined by XRD analysis. Figure 5 represents the XRD pattern of the $\text{Zn}_{1-x}\text{Cu}_x\text{O}$ ($x = 0.0, 1.5, 3.0,$ and 4.5%) nanorods. All the diffraction peaks corresponded to the hexagonal wurtzite structure with space group (P 63 m c) of the zinc oxide structure (match file no. 96–900-8878) with preferred orientation along (101) plane. The sharpness of the peaks revealed the purity of the wurtzite phase and well crystalline nature of the samples. With the substitution of Zn^{+2} by Cu^{+2} ions, the peak intensity increases, and a slight blue shift was observed. The increases in peak intensity correspond to more crystallinity of doped nanomaterial. It happened due to annealing at $500\text{ }^\circ\text{C}$ for 2 h in the electric furnace. The lattice constant was expanded from 3.238 to 3.242 \AA and no peaks were matched with CuO in the XRD pattern, which showed the absence of secondary phases.

The average crystallite size was found 29 nm, calculated by Debye-Scherrer's formula (Cullity 1956) using Eq. 3.

$$D = \frac{0.9\lambda}{\beta \cos\theta} \quad (3)$$

Crystal parameters like $a, c, c/a,$ unit cell volume, and bond length are given in Table 1.

Figure 6 shows the moving boundaries on attaching the Zn interstitials and substitutional copper ions, and the retardant force provides resistance to the moving particle's growth. If the driving force < the retarding force, the particle's growth does not occur further. So, Cu^{+2} ions

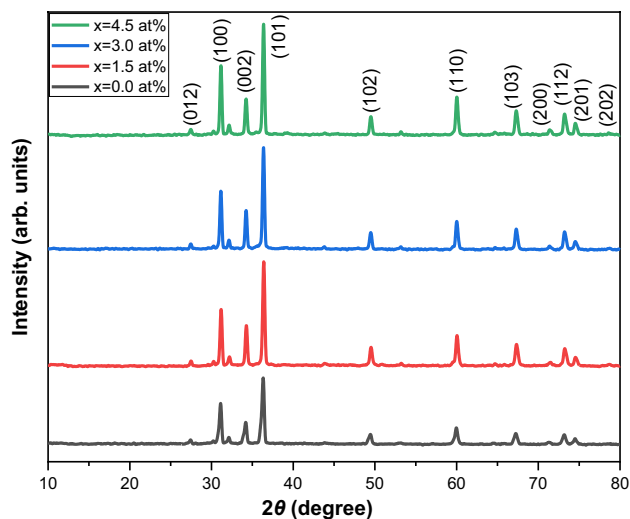
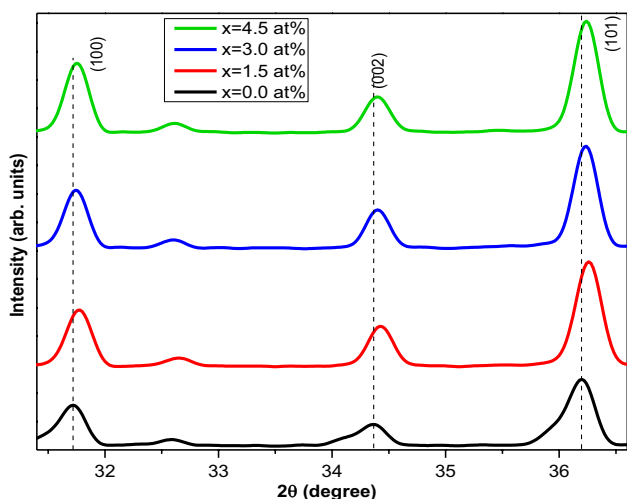


Fig. 5 XRD pattern of $\text{Zn}_{1-x}\text{Cu}_x\text{O}$ with varying dopant concentration

Table 1 Parameters calculated from XRD pattern of various dopant concentrations

Parameters	$Zn_{1-x}Cu_xO$			
	$x=0.0\%$	$x=1.5\%$	$x=3.0\%$	$x=4.5\%$
2θ (deg)	36.35	36.31	36.33	36.32
D (nm)	29.73	29.85	29.86	29.90
a (Å)	3.238	3.243	3.241	3.242
c (Å)	5.192	5.196	5.193	5.196
c/a	1.603	1.602	1.602	1.603
d -spacing (Å)	2.467	2.471	2.469	2.470
L (nm)	1.9712	1.9737	1.9725	1.9732
V (Å) ³	47.14	47.32	47.24	47.29

**Fig. 6** The shifting of (100) and (002) peaks with dopant concentration

prevented the growth of crystalline grains. The narrow width and highly intense peaks present in the X-ray diffractogram of the Cu-doped ZnO nanorods indicated that the nanorods were highly crystalline in nature.

SEM images of the samples are shown in Fig. 7. Nanorods of pure and Cu-doped ZnO NPs can be observed in the images (Fig. 7). Mostly, nanorods of ZnO are formed by the hydrothermal process because every oxygen ion (O^{2-}) and zinc ion (Zn^{2+}) in their respective planes are joined tetrahedrally with their four neighbors. Due to this ionic assembly, the crystal lacks central axis symmetry to reveal piezoelectric properties. So, the crystal owes polarization along the c -axis that makes the crystal lattice stable with the polar surfaces and it grows in rod-like morphology.

EDX analysis

EDX analysis was carried out to check the purity of samples synthesized by hydrothermal process. EDX spectra of the sample are shown in Fig. 8.

EDX spectra revealed the purity of the sample owing to the presence of peaks of copper, zinc, and oxygen. The absence of any other peaks has proved the 100% purity of samples with the given composition.

VSM analysis

VSM analysis was carried out to determine the ferromagnetic nature of samples at room temperature. In Fig. 9, the magnetization of samples was plotted as a function of the applied field ($M-H$) at room temperature, which showed the ferromagnetic nature of the synthesized materials. The hysteresis loop revealed that the remnant magnetization of Cu-doped sample increases with the increase of Cu concentration. Because of the doping, overlapping occurs between empty 3d orbitals of copper ions and donor electron states of ZnO at the Fermi level which introduces long-range ferromagnetic ordering. The coercivity also increases from 171.9 to 219.9 Oe for maximum dopant concentration. It is because of the domain-wall pinning process, in the crystal structure of doped samples, oxygen vacancies provide pinning sites to introduce domain-wall movement and enhance coercivity. The results showed the diamagnetic magnetic nature of ZnO NPs converted into ferromagnetic on Cu doping. Table 2

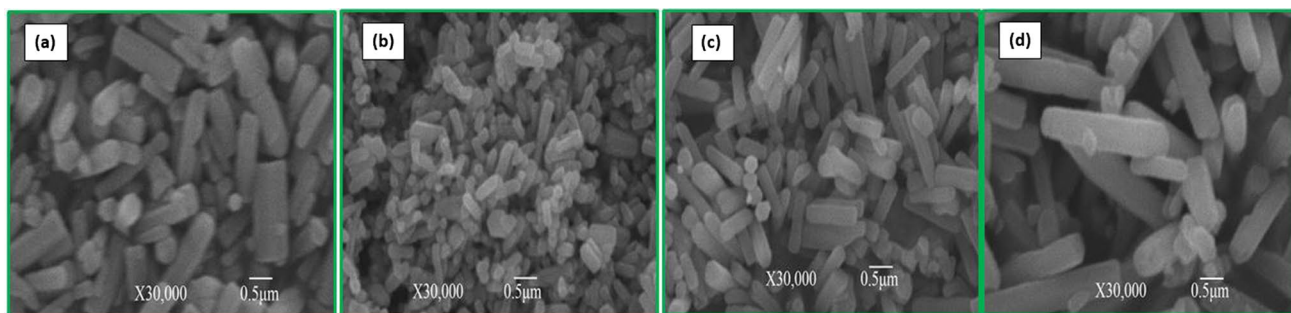
**Fig. 7** SEM micrographs of $Zn_{1-x}Cu_xO$ nanorods at **a** $x=0.0\%$, **b** $x=1.5\%$, **c** $x=3.0\%$, and **d** $x=4.5\%$

Fig. 8 EDX spectra of Cu-doped ZnO nanorods

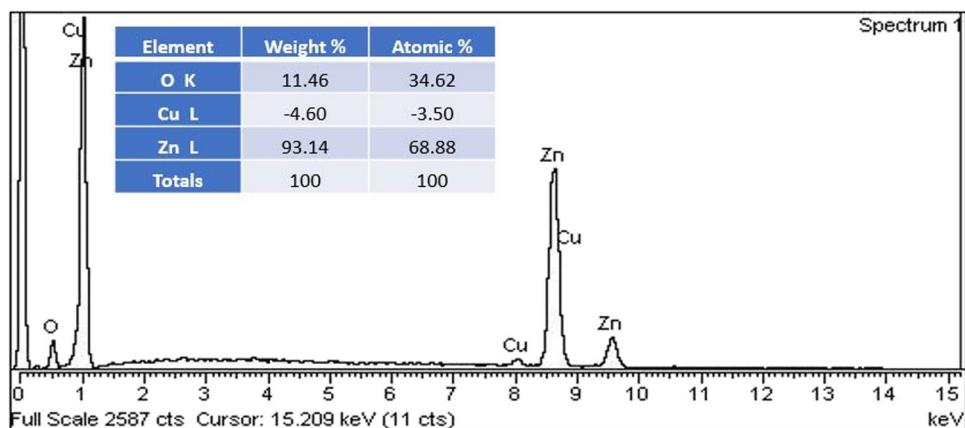
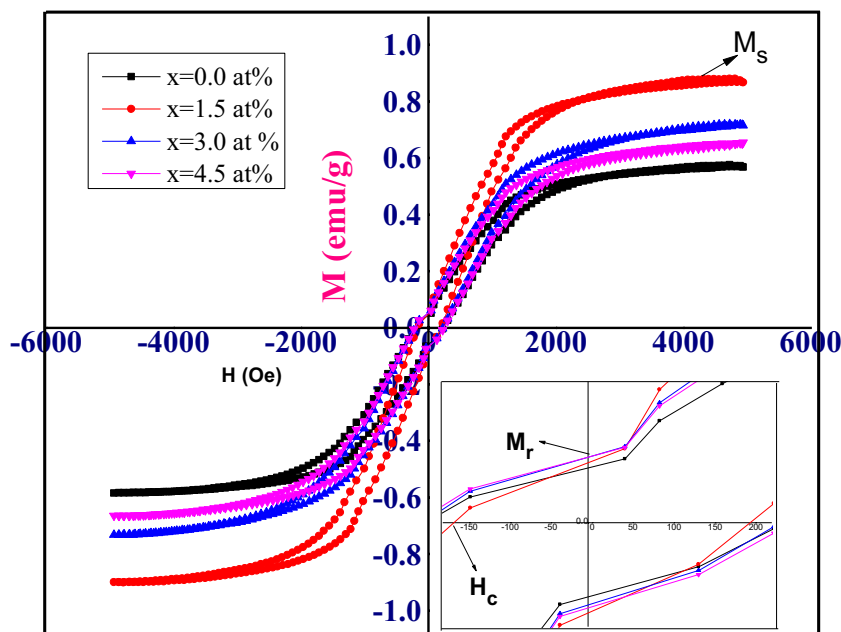


Fig. 9 Hysteresis loop for various dopant concentrations



shows the different parameters such as Curie temperature, saturation magnetization, remnant magnetization, and coercive field variation as the concentration of Cu was changed.

Electrical properties

The electrical properties of semiconductor ZnO nanorods can be significantly improved by the introduction of electron-rich noble metals like copper. Therefore, the effect of

Cu doping at various concentrations was observed on electrical properties. Figure 10(a) shows the variation of resistivity with temperature. This variation can be explained based on the exact location of cations in the microstructure of the crystal. If Cu^{2+} and Cu^{1+} exist at lattice sites due to electron hopping, so by Cu doping lattice expands and electron hopping possibility decreases; that is, DC conductivity decreases and resistivity increases. But with increasing temperature, hopping occurs and resistivity decreases, where T_c is the

Table 2 Magnetic properties of Cu-doped ZnO NPs

Dopant concentration x (at%)	Curie temperature T_c (K)	Saturation magnetization M_s (emu/g)	Remnant magnetization M_r (emu/g)	Coercive field H_c (Oe)
0.0	323	0.57	0.044	208.2
1.5	342.5	0.88	0.049	171.9
3.0	353	0.72	0.053	209
4.5	423.2	0.65	0.053	219.9

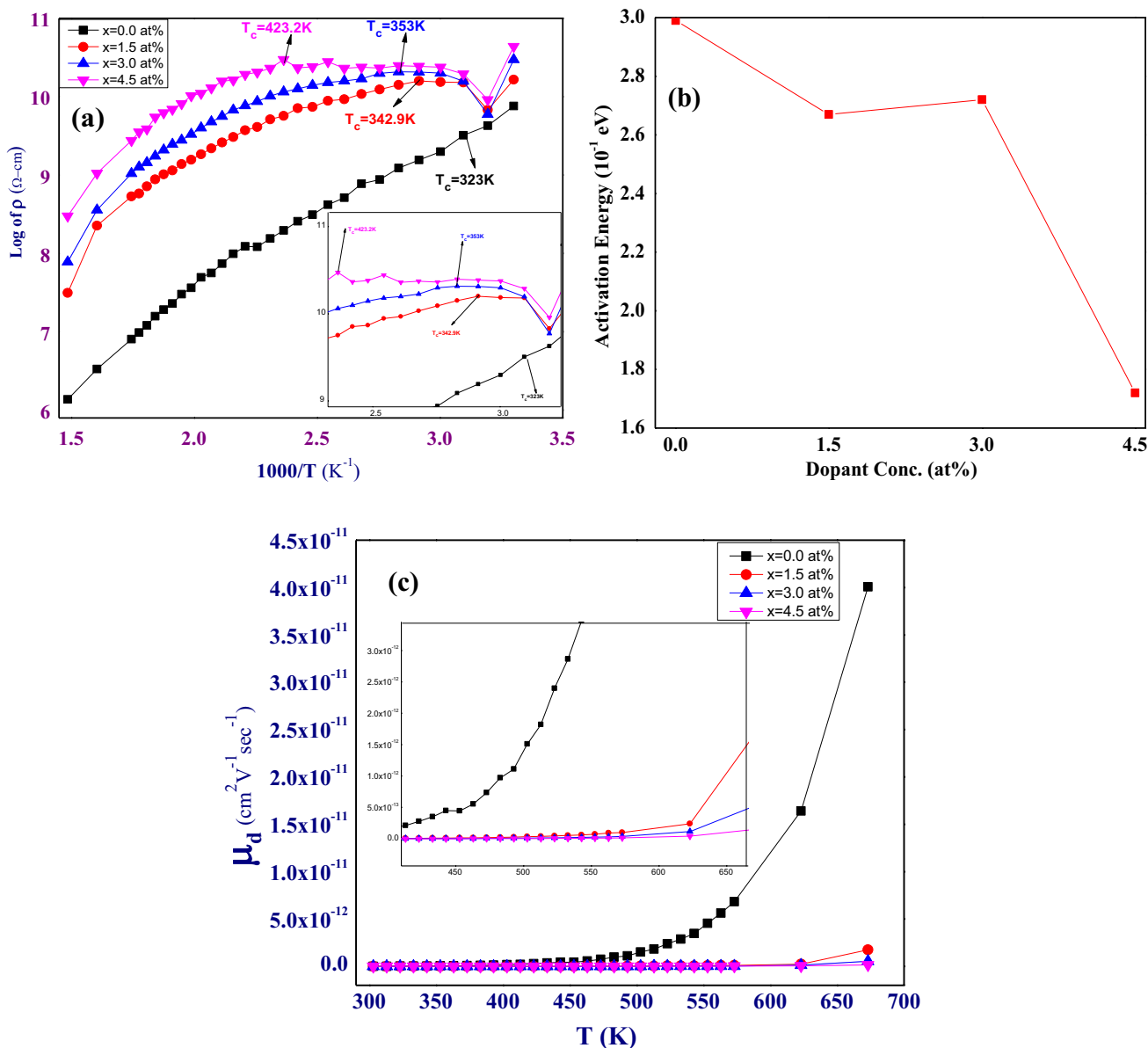


Fig. 10 a Variation of resistivity with temperature for several dopant concentrations. b Variation of activation energy with dopant concentration. c Variation of drift mobility with temperature for several dopant concentrations

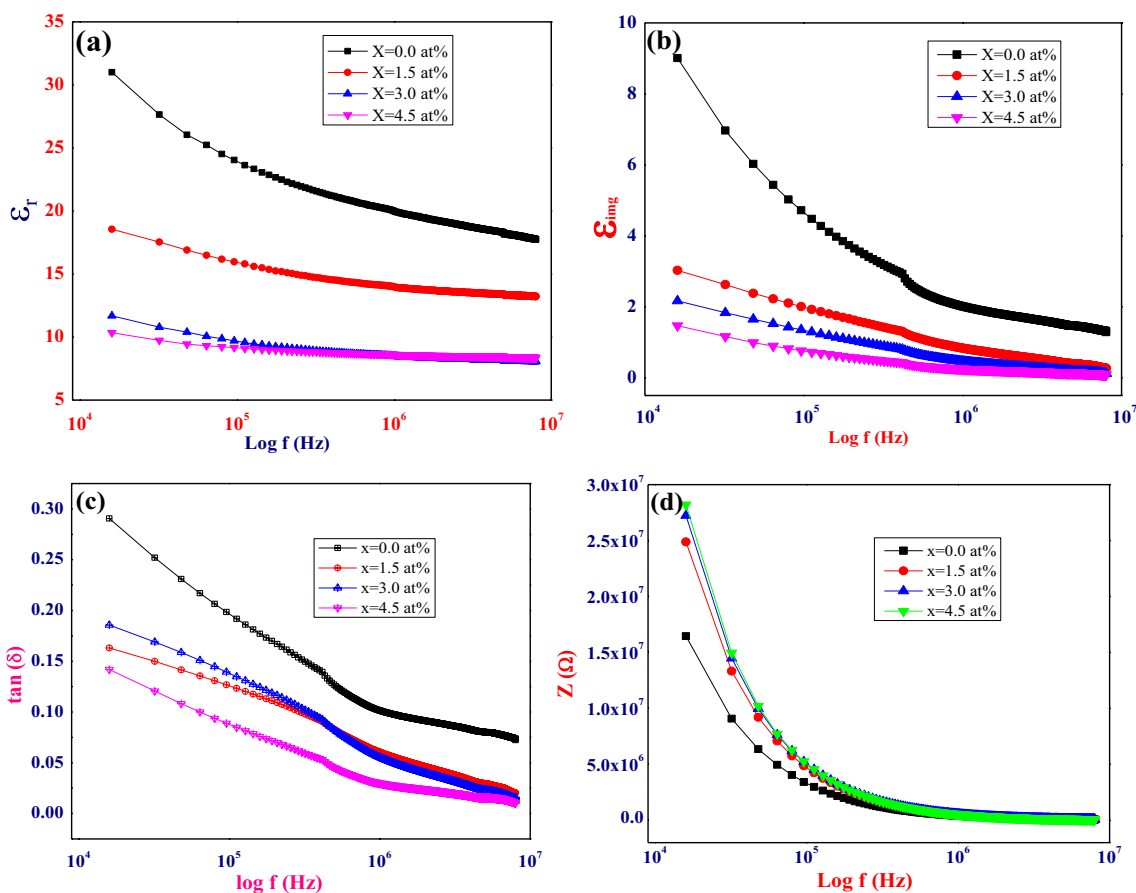
Curie temperature that increases with doping concentration. In Fig. 10(b), the activation energy is much influenced by the carrier concentration of the donor and impurity’s energy levels. An increase in donor amount (increment in Cu doping) shifts the Fermi level up in the energy gap which reduces the activation energy. Figure 10(c) shows that the resistivity increases with Cu doping and the mobility of charge carriers decreases. Drift mobility is less at low temperatures and increases sharply at high temperatures. Table 3 shows the I–V measurement of different doped samples and how DC conductivity, activation energy, and drift mobility vary with various concentrations of Cu.

Dielectric properties

Dielectric properties are useful parameters for the applications of nanomaterials in supercapacitors. Figure 11 (a) and (b) show the higher value of relative permittivity and ϵ_{img} for all samples at low frequency ‘ f ’, due to the dominant effect of oxygen and grain boundary defects because defects contributing to polarizability lags the electric field at high f . In Cu-doped ZnO samples, the electrons shifting dominate between Cu and Zn ions at low f . When the electric field frequency is lower, charge carriers hopping between Cu and Zn ions occur and electrons follow the electric field. So, higher tangent loss

Table 3 Different parameters found from I–V measurement of $Zn_{1-x}Cu_xO$

Electrical parameters	$Zn_{1-x}Cu_xO$			
	$x=0.0\%$	$x=1.5\%$	$x=3.0\%$	$x=4.5\%$
DC conductivity σ_{DC} ($\Omega^{-1} \text{ cm}^{-1}$)	7.31×10^{-7}	3.2×10^{-8}	1.28×10^{-8}	3.34×10^{-9}
Activation energy E_{act} (eV)	0.299	0.267	0.273	0.172
Drift mobility μ_d ($\text{cm}^2 \text{ V}^{-1} \text{ s}^{-1}$)	4.01×10^{-11}	1.73×10^{-12}	5.44×10^{-13}	1.57×10^{-13}

**Fig. 11** Dielectric properties of Cu-doped ZnO NPs: **a** real, **b** imaginary, **c** dielectric tangent loss factor, and **d** impedance vs. frequency

' $\tan(\delta)$ ' and ϵ_r are observed at low f as shown in Fig. 10 (a) and (c) as intrinsic donor defects reduce at high Cu doping which provides an impedance to reduce ϵ_r . From XRD results, more porosity and density reduce ϵ_r , ϵ_{img} , and $\tan(\delta)$. Impedance analysis reveals that AC conductivity reduces with Cu doping, so an inverse process occurs for impedance analysis as impedance increases with Cu doping as shown in Fig. 10(d).

AC conductivity

AC conductivity of pure and doped ZnO NPs slightly depends upon frequency. Figure 12 indicates that the AC conductivity of ZnO NPs increases with frequency and shows a decrement in AC electrical conductivity with increasing Cu doping. The larger copper atoms in

grain act as a barrier to trap charge carriers which in turn decrease electrical mobility. However, more Cu ions would get segregated at the grain boundaries when the doping level of Cu is high. So, the density of electrical carriers at the grain boundaries would be high, the resistance of the grain boundaries would be reduced, and the barrier height would decrease. Thus, the AC conductivity is improved with an increased amount of Cu doping in ZnO.

The anti-bacterial potential of $Zn_{1-x}Cu_xO$ nanorods

The anti-bacterial potential of $Zn_{1-x}Cu_xO$ nanorods evaluated by the disk diffusion method revealed the noxious nature of these particles against both strains, gram-positive and gram-negative bacteria (Table 4). It was observed that

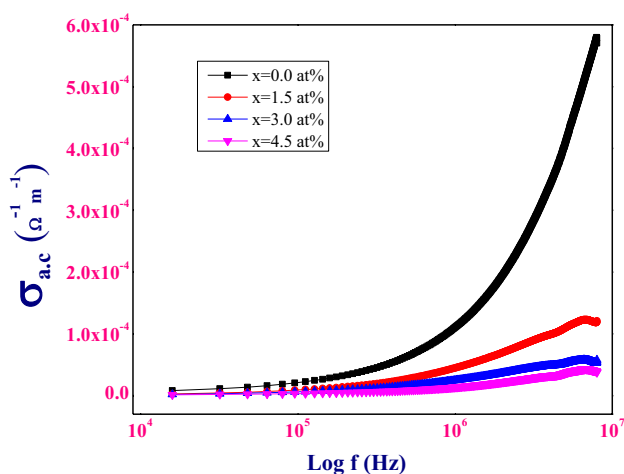


Fig. 12 Variation of AC conductivity with frequency for different dopant concentrations

the anti-bacterial activity of doped ZnO NPs increased with an increase in dopant concentration. Moreover, the doped NPs were found more active against gram-negative strains of bacteria as compared to gram-positive which may be attributed to the relatively thin cell wall of these strains. The outer cell wall of gram-positive bacteria is relatively thick which prevents the crossing of NPs into the cell. On crossing the membrane barrier, NPs may interact with the genetic material of the cell or inhibit the enzyme actions which ultimately ceases bacterial growth. The comparative anti-bacterial potential of Zn_{1-x}Cu_xO is represented in Fig. 13.

Photocatalytic activity

Photocatalysis is an effective way to degrade dyes and other water pollutants by light irradiation. Appropriate band gap between conduction and valence band permits the photoexcitation of electrons to degrade the dyes. In this regard, the photodegradation of MO dyes was studied employing the prepared nanorods as the photocatalysts. It was observed that

Table 4 Measured ZOI for Zn_{1-x}Cu_xO samples with different types of bacteria

Dopant concentration	Zone of inhibition (nm)			
	Gram-positive bacteria		Gram-negative bacteria	
	<i>S. aureus</i>	<i>B. subtilis</i>	<i>E. coli</i>	<i>P. multocida</i>
x=0.0%	5 ± 0.3	5 ± 0.1	5 ± 0.2	5 ± 0.3
x=1.5%	7 ± 0.2	7.5 ± 0.3	10 ± 0.3	10.5 ± 0.2
x=3.0%	8 ± 0.2	9 ± 0.2	12 ± 0.2	12 ± 0.5
x=4.5%	10 ± 0.2	11 ± 0.2	15 ± 0.5	16 ± 0.3
Rifampicin (standard)	26 ± 0.6	24 ± 1.0	28 ± 0.4	28 ± 0.7

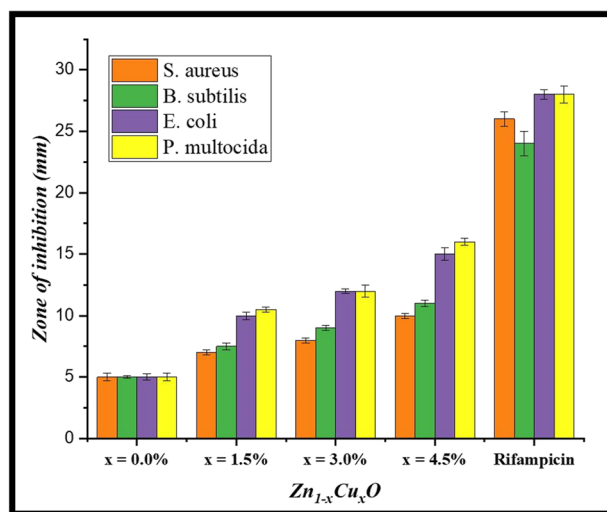


Fig. 13 Comparative chart of anti-bacterial activities of samples

the % dye degradation goes on increasing with an increase in dopant concentration which may be attributed to the more availability of electrons in the conduction band of ZnO due to doping as shown in Fig. 14(a).

Kinetic insight into the degradation reaction revealed that the reaction followed the pseudo-first-order kinetics and the rate constant was found to increase with the increase of dopant concentration as shown in Fig. 14(b). At pH 3 and 10-cm distance from the lamp, the maximum rate constant (*k*) was found to be -0.019 min⁻¹ when the dopant concentration was 4.5%.

For a better understanding of the mechanism and effect of reaction parameters, the degradation of MO dye was investigated using Zn_{1-x}Cu_xO (x = 4.5%) nanorods at varying reaction conditions by applying one-parameter one-time approach. Results are provided in Fig. 15.

Effect of pH

Figure 15(a) shows the effect of pH on catalytic efficiency to degrade MO dye. The surface charge of NPs can be modified by changing the pH of the media. A decrease in the pH of media produces a positive charge on the surface and vice versa (Sajid et al. 2020). Since MO is an anionic dye, a decrease in pH facilitates the adsorption of dye on the catalyst surface and enhances the degree of degradation. A significant decrease of % dye degradation was observed for Cu-doped ZnO NPs (x = 4.5%) at the same time interval (90 min) and catalyst dosage (0.5 g) with the increase of pH above 7 due to negative charge on the surface which reduces the adsorption of dye. At pH 11, the degradation potential was further reduced because, at this pH, ZnO NPs may be ionized to ZnO₂⁻ ions. Maximum degradation was observed at pH 3 due to a positively charged surface.

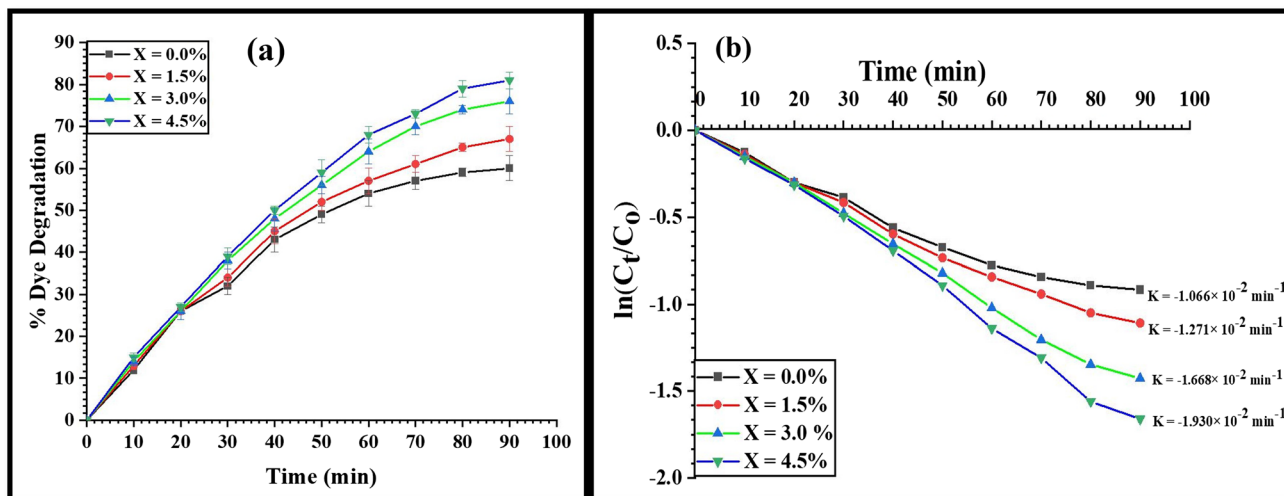


Fig. 14 Degradation of MO dye: a impact of time and b kinetic plot

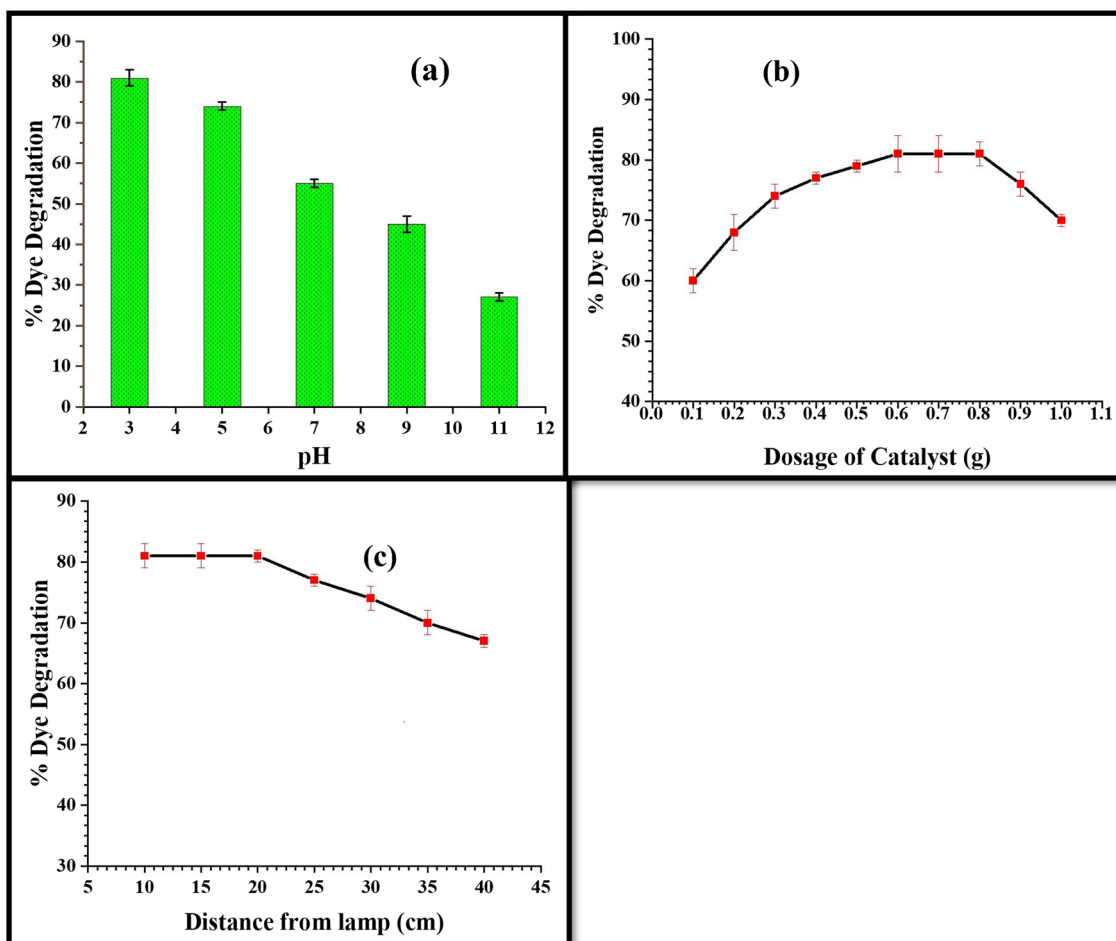


Fig. 15 Optimization of process parameters. Effect of a pH, b catalyst doze, and c light intensity

Effect of catalyst dosage

Figure 15(b) shows the effect of catalyst dosage on catalytic efficiency to degrade MO dye. Results illuminated that an increase in catalyst dose increases the dye removal efficiency. Increasing the amount from 0.1 to 0.5 g increased the degradation efficiency (Fig. 15(b)). After this, a constant period can be noted which then decreases on increasing catalyst dose beyond 0.8 g. Increasing the amount of catalyst increased the active sites in the media, which ultimately adsorb pollutants and degrade and desorb back into the solution. After a certain catalyst dosage (> 0.8 g), a decrease of % dye degradation was observed which may be due to aggregation of NPs at high concentrations. Additionally, the high catalyst concentration impacted the penetration of light negatively due to high turbidity which made the solution opaque solution.

Effect of light intensity

The impact of light on dye degradation is shown in Fig. 15(c). The impact was varied by increasing/decreasing the distance of the light source from the experimental solution. It can be observed from Fig. 15(c) that light intensity has a minor effect on dye degradation. A slight decrease in % degradation was observed with a decrease in light intensity (with an increase in distance from the lamp) and vice versa. The band gap sensitization mechanism is not affected by the intensity of light.

Proposed mechanism

Based on the experimental results and literature shreds of evidence, the degradation of MO dye has proceeded through the following mechanism (Batra et al. 2022; Ajmal et al. 2014).

Photoexcitation

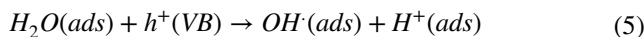
The photocatalytic reaction is initiated by the absorption of photons of incident light on the catalyst. Electron absorbs the photon of incident light equal to or greater than the band gap and jumps to the conduction band from the valence band. As a result, electron–hole pair is generated, indicated by Eq. 4.



Ionization of water

Electron-deficient holes in the valence band of NP react with the water molecule to produce hydroxyl radicals (Eq. 5) which are strong oxidizing agents. These reacting agents react with MO molecules (or any organic pollutants) non-selectively and rupture the bonds. This rupturing

of molecules produces other reactive species by molecular decomposition. The produced reacting species may also attack microorganisms such as bacteria by rupturing their cell barriers resulting in their deactivation and cease their growth ultimately.



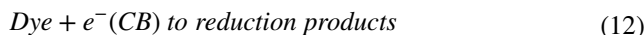
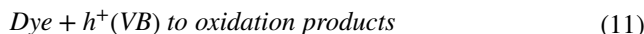
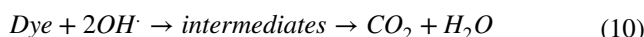
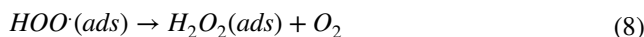
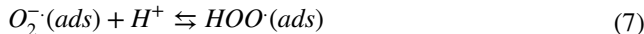
Oxygen ionosorption

Oxygen being highly electronegative in nature can easily accept electron present in the conduction band to form anionic superoxide radical as shown in Eq. 6. This radical is a strong oxidizing agent which may cause further oxidation of pollutant species. Formation of this radical by accepting the electron also prevents the recombination of electron–hole pairs.



Protonation of superoxide

Superoxide radical reacts with hydrogen ions to produce multiple oxidizing species by chain reactions as represented in Eqs. 7–12. All these species can break down the organic structures present/adsorb on the surface of NPs.



Recovery and recycling

Regeneration of the catalyst was carried out to check the reusability of the catalyst several times. In this regard, the catalyst was regenerated five times after successive uses. After every use, the mixture was centrifuged for 20 min at 5000 rpm to recover the catalyst. The supernatant liquid was discarded and the remaining mixture was rinsed with distilled water three times. After washing, NPs were oven dried at 60 °C for 5 h (Ranjith and Kumar 2017). After five-time uses, a very slight decrease (11%) in the activity

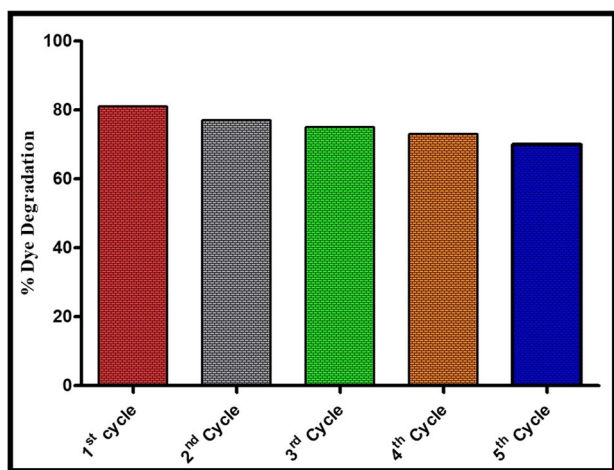


Fig. 16 Cycling stability of the prepared catalyst

of the catalyst was observed for the degradation of the dye as shown in Fig. 16. Hence, it was believed that this catalyst can be reused after robust regeneration to purify the wastewater with minimum loss in activity.

Conclusion

$Zn_{1-x}Cu_xO$ ($x=0\%$, 1.5% , 3.0% , and 4.5%) nanorods were fabricated through the hydrothermal method with different dopant concentrations. All synthesized samples have exhibited hexagonal crystal structure and the crystallinity of samples was improved with increasing dopant concentration. SEM images revealed the nanorod-like morphology of samples. UV–Visible spectra revealed a red shift in the optical band gap from 3.14 to 2.7 eV and FTIR analysis confirmed the purity and presence of only Zn–O and O–H bonds in the samples. The purity of samples was further confirmed by the EDX analysis. The dielectric properties of all samples were studied from kHz to MHz frequency range and noted that Cu doping decreased the dielectric constant and tangent loss while improving the impedance. The AC conductivity decreases with an increase in Cu dopant concentration. DC measurements results illuminated an increase in resistivity and drift mobility with improved dopant concentration. Moreover, magnetic properties, remnant magnetization, and coercivity upgraded with increasing dopant concentration. All the samples were found biologically active against gram-positive and gram-negative strains of bacteria with maximum inhibition with highly doped nanorods. The photocatalytic activity was also improved with increasing Cu content due to a red shift in the energy band gap. The effect of pH and catalyst dosage revealed the maximum % MO degradation at pH 3 using a 0.6-g catalyst. Moreover, the reusability study of catalyst has shown a slight decrease in catalyst activity after five cycles.

Acknowledgements We acknowledge the support provided by the Higher Education Commission of Pakistan and Huaiyin Institute of Technology, Huaian China to complete this study.

Author contribution All authors contributed to the study's conception and design. Material preparation, data collection, and analysis were performed by Yasir Zaman, M. Zahid Ishaque, Yasir Yousaf, Abu Bakar Siddique, and M. Shahzad. The first draft of the manuscript was written by Abu Bakar Siddique and Muhammad Imran Arshad. Analyses were performed by Muhammad Sajid and Ghulam Nabi. The work performed was supervised by Yasir Zaman, Abu Bakar Siddique, and Nisar Ali. All authors read and approved the final manuscript.

Funding This work was financially supported by Higher Education Commission Start-up research grant Program No: 21–2079/SRGP/R&D/HEC/2018; Key Laboratory of Regional Resource Exploitation and Medicinal Research, project numbers LPRK201909 and LPRK202101; and Jiangsu Province College Students' Innovation and Entrepreneurship Training program, project numbers 202111049338 and 202111049352.

Data availability All the data is available in the manuscript. Additional information/data can be provided on request.

Declarations

Ethical approval Not applicable.

Consent to participate Not applicable.

Consent for publication All the authors have read and agreed to publish this study.

Competing interests The authors declare no competing interests.

References

- Ahmed A, Usman M, Yu B, Shen Y, Cong H (2021) Sustainable fabrication of hematite ($\alpha\text{-Fe}_2\text{O}_3$) nanoparticles using biomolecules of *Punica granatum* seed extract for unconventional solar-light-driven photocatalytic remediation of organic dyes. *J Mol Liq* 339:116729. <https://doi.org/10.1016/j.molliq.2021.116729>
- Ajmal A, Majeed I, Malik RN, Idriss H, Nadeem MA (2014) Principles and mechanisms of photocatalytic dye degradation on TiO_2 based photocatalysts: a comparative overview. *RSC Adv* 4(70):37003–37026. <https://doi.org/10.1039/C4RA06658H>
- Ali N, Zhang B, Zhang H, Li W, Zaman W, Tian L, Zhang Q (2015) Novel Janus magnetic micro particle synthesis and its applications as a demulsifier for breaking heavy crude oil and water emulsion. *Fuel* 141:258–267. <https://doi.org/10.1016/j.fuel.2014.10.026>
- Ali N, Riead MMH, Bilal M, Yang Y, Khan A, Ali F, Iqbal HM (2021a) Adsorptive remediation of environmental pollutants using magnetic hybrid materials as platform adsorbents. *Chemosphere* 284:131279. <https://doi.org/10.1016/j.chemosphere.2021.131279>
- Ali A, Ahmed A, Usman M, Raza T, Ali MS, Al-Nahari A, Li C (2023) Synthesis of visible light responsive $\text{CeO}_2/\text{CoO} \cdot 8\text{Fe}_2\text{O}_4/\text{g-C}_3\text{N}_4$ composites for efficient photocatalytic degradation of rhodamine B. *Diamond Relat Mater* 133:109721. <https://doi.org/10.1016/j.diamond.2023.109721>
- Ali N, Khan A, Bilal M, Malik S, Badshah S, Iqbal H (2020) Chitosan-based bio-composite modified with thiocarbamate moiety for decontamination of cations from the aqueous media. *Molecules* 25(1):226. <https://doi.org/10.3390/molecules25010226>

- Ali N, Bilal M, Khan A, Ali F, Khan H, Khan HA, Iqbal HM (2021b) Fabrication strategies for functionalized nanomaterials. In *Nanomaterials: Synthesis, Characterization, Hazards and Safety* (pp. 55–95). Elsevier. <https://doi.org/10.1016/B978-0-12-823823-3.00010-0>
- Anjum S, Hashim M, Malik SA, Khan M, Lorenzo JM, Abbasi BH, Hano C (2021) Recent advances in zinc oxide nanoparticles (Zn NPs) for cancer diagnosis, target drug delivery, and treatment. *Cancers* 13(18):4570. <https://doi.org/10.3390/cancers13184570>
- Batra V, Kaur I, Pathania D, Chaudhary V (2022) Efficient dye degradation strategies using green synthesized ZnO-based nanoplat-forms: a review. *Appl Surface Sci Adv* 11:100314. <https://doi.org/10.1016/j.apsadv.2022.100314>
- Çolak H, Karaköse E (2022) Gadolinium (III)-doped ZnO nanorods and gas sensing properties. *Mater Sci Semicond Process* 139:106329. <https://doi.org/10.1016/j.mssp.2021.106329>
- Cullity BD (1956) *Elements of X-ray diffraction*. Addison-Wesley Publishing
- Gan YX, Jayatissa AH, Yu Z, Chen X, Li M (2020) Hydrothermal synthesis of nanomaterials. *J Nanomater* 2020:1–3. <https://doi.org/10.1155/2020/8917013>
- Ge Z, Wang C, Chen T, Chen Z, Wang T, Guo L, Liu J (2021) Preparation of Cu-doped ZnO nanoparticles via layered double hydroxide and application for dye-sensitized solar cells. *J Phys Chem Solids* 150:109833. <https://doi.org/10.1016/j.jpcs.2020.109833>
- Guoliang Y, Fang D, Chowdhury A, Aixin Z, and Sajid M (2022) Persistent organic pollutants in Chinese waterways: occurrence, remediation, and epidemiological perspectives. 56:102688. <https://doi.org/10.1016/j.risma.2022.102688>
- Ishaque MZ, Zaman Y, Shahzad M, Siddique AB, Shahid S, Akram M, Hussain S (2023) Photocatalytic and antibacterial potential of silver nanocubes and nanorods synthesized via polyol reduction method. *Water Air Soil Pollut* 234(4):252. <https://doi.org/10.1007/s11270-023-06269-w>
- Jabbar I, Zaman Y, Althubeiti K, Al Otaibi S, Ishaque MZ, Rahman N, ... Khan A (2022) Diluted magnetic semiconductor properties in TM doped ZnO nanoparticles. *RSC Adv* 12(21):13456–13463. <https://doi.org/10.1039/D2RA01210C>
- Kant R, Sharma D, Bansal A, Singh R (2021) Structural, optical and dielectric properties of Al/Mn doped ZnO nanoparticles, a comparative study. *Mater Technol* 36(9):513–520. <https://doi.org/10.1080/10667857.2020.1775408>
- Kotresh MG, Patil MK, Inamdar SR (2021) Reaction temperature based synthesis of ZnO nanoparticles using co-precipitation method: detailed structural and optical characterization. *Optik* 243:167506. <https://doi.org/10.1016/j.jijleo.2021.167506>
- Kumbhakar P, Gowda CC, Mahapatra PL, Mukherjee M, Malviya KD, Chaker M, Tiwary CS (2021) Emerging 2D metal oxides and their applications. *Mater Today* 45:142–168. <https://doi.org/10.1016/j.mattod.2020.11.023>
- Maqbool S, Ahmed A, Mukhtar A, Jamshaid M, Rehman AU, Anjum S (2023) Efficient photocatalytic degradation of Rhodamine B dye using solar light-driven La-Mn co-doped Fe₂O₃ nanoparticles. *Environ Sci Pollut Res* 30(3):7121–7137. <https://doi.org/10.1007/s11356-022-22701-w>
- Mortezaghali B, Movahed E, Fathi A, Soleimani M, Forutan Mirhosseini A, Zeini N, ... Zareanshahraki M (2022) Plant-mediated synthesis of silver-doped zinc oxide nanoparticles and evaluation of their antimicrobial activity against bacteria cause tooth decay. *Microsc Res Tech* 85(11):3553–3564. <https://doi.org/10.1002/jemt.24207>
- Muktariidha O, Adlim M, Suhendrayatna S, Ismail I (2021) Progress of 3d metal-doped zinc oxide nanoparticles and the photocatalytic properties. *Arab J Chem* 14(6):103175. <https://doi.org/10.1016/j.arabjc.2021.103175>
- Naik EI, Naik HB, Viswanath R, Kirthan BR, Prabhakara MC (2020) Effect of zirconium doping on the structural, optical, electrochemical and antibacterial properties of ZnO nanoparticles prepared by sol-gel method. *Chem Data Collect* 29:100505. <https://doi.org/10.1016/j.cdc.2020.100505>
- Nagaraju G, Prashanth SA, Shastri M, Yathish KV, Anupama C, Rangappa DJMRB (2017) Electrochemical heavy metal detection, photocatalytic, photoluminescence, biodiesel production and antibacterial activities of Ag–ZnO nanomaterial. *Mater Res Bull* 94:54–63. <https://doi.org/10.1016/j.materresbull.2017.05.043>
- Neamen DA (1992) *Semiconductor physics and devices basic principles*. Tata McGraw Hill Publishing
- Ramírez AE, Montero-Muñoz M, López LL, Ramos-Ibarra JE, Coaquira JA, Heinrichs B, Páez CA (2021) Significantly enhancement of sunlight photocatalytic performance of ZnO by doping with transition metal oxides. *Sci Rep* 11(1):1–9. <https://doi.org/10.1038/s41598-020-78568-9>
- Ranjith KS, Kumar RR (2017) Regeneration of an efficient, solar active hierarchical ZnO flower photocatalyst for repeatable usage: controlled desorption of poisoned species from active catalytic sites. *RSC Adv* 7(9):4983–4992. <https://doi.org/10.1039/C6RA27380G>
- Sattara R, Rasoola MA, Qadirb R, Siddiqueb AB, Irfanb MI, Sabac I, ... Mustaqeemb M (2023) Biogenic synthesis of zinc oxide nanoparticles using leaves extract of *Camellia sinensis* for photocatalytic and biological applications. *J Optoelectron Biomed Mater* 15(1):1–9. <https://doi.org/10.15251/JOEBM.2023.151.1>
- Sajid M, Bari S, Rehman MS, Ashfaq M, Guoliang Y, Mustafa G (2022) Adsorption characteristics of paracetamol removal onto activated carbon prepared from *Cannabis sativum* Hemp. *Alex Eng J* 61(9):7203–7212. <https://doi.org/10.1016/j.aej.2021.12.060>
- Sajid M, Ahmad MI, Shafiq SS, Pasha MK, Asim M (2020) Decolorization of azo dyes: C.B-10X Blue and C.B.M-10X Blue by ozonation for waste water treatment. *Univ Wah J Sci Technol* 4(1):1–7 (<http://uwjst.org.pk/index.php/uwjst/article/view/49>)
- Saber NB, Mezni A, Alrooqi A, Altalhi T (2020) A review of ternary nanostructures based noble metal/semiconductor for environmental and renewable energy applications. *J Market Res* 9(6):15233–15262. <https://doi.org/10.1016/j.jmrt.2020.10.090>
- Salam M, Alam F, Dezhi S, Nabi G, Shahzadi A, Hassan SU, Bilal M (2021) Exploring the role of Black Soldier Fly Larva technology for sustainable management of municipal solid waste in developing countries. *Environ Technol Innov* 24:101934. <https://doi.org/10.1016/j.eti.2021.101934>
- Shkir M, Palanivel B, Khan A, Kumar M, Chang JH, Mani A, AlFaify S (2022) Enhanced photocatalytic activities of facile auto-combustion synthesized ZnO nanoparticles for wastewater treatment: an impact of Ni doping. *Chemosphere* 291:132687. <https://doi.org/10.1016/j.chemosphere.2021.132687>
- Shi Y, Liu QG, Chen Y, Wang MH (2021) Structure, optical and varistor properties of one-dimensional Co-doped ZnO synthesized by reflux method. *J Electron Mater* 50(10):5891–5897. <https://doi.org/10.1007/s11664-021-09106-0>
- Siddique AB, Ahmad S, Shaheen MA, Ali A, Tahir MN, Vieira LC, Siddeeg SM (2022) Synthesis, antimicrobial potential and computational studies of crystalline 4-bromo-2-(1,4,5-triphenyl-1 H-imidazole-2-yl) phenol and its metal complexes. *CrystEngComm* 24(47):8237–8247. <https://doi.org/10.1039/D2CE01118B>
- Tariq M et al (2023) O-vacancies induced in co-doped ZnO:(Cu, Fe) synthesized via hydrothermal method by pulsed magnetic field. *Mater Sci Eng: B* 294(2023):116549. <https://doi.org/10.1016/j.mseb.2023.116549>
- Usman M, Ahmed A, Ji Z, Yu B, Rafiq M, Shen Y, Cong H (2022) Enhanced heterogenous photo-Fenton degradation of tetracycline in aqueous medium by visible light responsive sulphur doped


- zinc ferrite nanoparticles. *Mater Today Chem* 26:101003. <https://doi.org/10.1016/j.mtchem.2022.101003>
- Wu SH, Xue H, Yang C, Cheng PM, Zhang P, Kuang J, Sun J (2021) Effect of Si addition on the precipitation and mechanical/electrical properties of dilute Al–Zr–Sc alloys. *Mater Sci Eng: A* 812:141150. <https://doi.org/10.1016/j.msea.2021.141150>
- Zaman Y, Ishaque MZ, Sattar R, Rehman MM, Saba I, Kanwal S, Siddique AB (2022) Antibacterial potential of silver nanoparticles synthesized using tri-sodium citrate via controlled exploitation of temperature. *Digest J Nanomater Biostructures* 17(3):979–987. <https://doi.org/10.15251/DJNB.2022.173.979>
- Zaman Y, Ishaque MZ, Ajmal S, Shahzad M, Siddique AB, Hameed MU, Yasin G (2023) Tamed synthesis of AgNPs for

photodegradation and anti-bacterial activity: effect of size and morphology. *Inorg Chem Commun* 150:110523. <https://doi.org/10.1016/j.inoche.2023.110523>

Publisher's note Springer Nature remains neutral with regard to jurisdictional claims in published maps and institutional affiliations.

Springer Nature or its licensor (e.g. a society or other partner) holds exclusive rights to this article under a publishing agreement with the author(s) or other rightsholder(s); author self-archiving of the accepted manuscript version of this article is solely governed by the terms of such publishing agreement and applicable law.

Authors and Affiliations

Yasir Zaman¹ · Muhammad Zahid Ishaque¹ · Yasir Yousof¹ · Muhammad Shahzad¹ · Abu Bakar Siddique² · Muhammad Imran Arshad³ · Muhammad Sajid⁴  · Nisar Ali⁵ · Ghulam Nabi⁶

✉ Muhammad Sajid
engr.sajid80@gmail.com; drsajid@nenu.edu.cn

¹ Department of Physics, University of Sargodha, Sargodha 40100, Pakistan

² Institute of Chemistry, University of Sargodha, Sargodha 40100, Pakistan

³ Department of Physics, Government College University Faisalabad, Faisalabad, Pakistan

⁴ National & Local United Engineering Laboratory for Power Batteries, College of Chemistry, Northeast Normal University, Changchun, Jilin 130024, China

⁵ Key Laboratory for Palygorskite Science and Applied Technology of Jiangsu Province, National & Local Joint Engineering Research Center for Deep Utilization Technology of Rock-Salt Resource, Faculty of Chemical Engineering, Huaiyin Institute of Technology, Huaian 223003, China

⁶ Institute of Nature Conservation, Polish Academy of Sciences, Krakow, Poland